Neurobiology of Disease 183 (2023) 106177

Contents lists available at ScienceDirect

Neurobiology of Disease

journal homepage: www.elsevier.com/locate/ynbdi

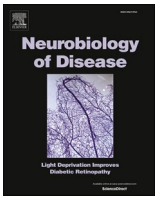

Missense mutations in the membrane domain of PRRT2 affect its interaction with Nav1.2 voltage-gated sodium channels

Bruno Sterlini [a,b,1], Francesca Franchi [b,c,1], Lisastella Morinelli [a,b,1], Beatrice Corradi [a,b], Chiara Parodi [a], Martina Albini [a], Alessandra Bianchi [a], Antonella Marte [a], Pietro Baldelli [a,c], Giulio Alberini [b,c], Luca Maragliano [b,d], Pierluigi Valente [a,b], Fabio Benfenati [b,c,*,1], Anna Corradi [a,c,**,1]

[a] Department of Experimental Medicine, University of Genova, Viale Benedetto XV, 3, Genova 16132, Italy
[b] Center for Synaptic Neuroscience and Technology, Istituto Italiano di Tecnologia, Largo Rosanna Benzi 10, Genova 16132, Italy
[c] IRCCS Ospedale Policlinico San Martino, Largo Rosanna Benzi 10, Genova 16132, Italy
[d] Department of Life and Environmental Sciences, Polytechnic University of Marche, Ancona, Italy

ARTICLE INFO

Keywords:
Proline-rich transmembrane protein-2
Voltage-dependent sodium channels
Molecular dynamics
Intrinsic excitability
Paroxysmal kinesigenic dyskinesia

ABSTRACT

PRRT2 is a neuronal protein that controls neuronal excitability and network stability by modulating voltage-gated Na^+ channel (Nav). PRRT2 pathogenic variants cause pleiotropic syndromes including epilepsy, paroxysmal kinesigenic dyskinesia and episodic ataxia attributable to loss-of-function pathogenetic mechanism. Based on the evidence that the transmembrane domain of PRRT2 interacts with Nav1.2/1.6, we focused on eight missense mutations located within the domain that show expression and membrane localization similar to the wild-type protein. Molecular dynamics simulations showed that the mutants do not alter the structural stability of the PRRT2 membrane domain and preserve its conformation. Using affinity assays, we found that the A320V and V286M mutants displayed respectively decreased and increased binding to Nav1.2. Accordingly, surface biotinylation showed an increased Nav1.2 surface exposure induced by the A320V mutant. Electrophysiological analysis confirmed the lack of modulation of Nav1.2 biophysical properties by the A320V mutant with a loss-of-function phenotype, while the V286M mutant displayed a gain-of-function with respect to wild-type PRRT2 with a more pronounced left-shift of the inactivation kinetics and delayed recovery from inactivation. The data confirm the key role played by the PRRT2-Nav interaction in the pathogenesis of the PRRT2-linked disorders and suggest an involvement of the A320 and V286 residues in the interaction site. Given the similar clinical phenotype caused by the two mutations, we speculate that circuit instability and paroxysmal manifestations may arise when PRRT2 function is outside the physiological range.

1. Introduction

PRRT2 is a neuron-specific protein that plays important roles in the control of intrinsic excitability and synaptic transmission (Valtorta et al., 2016; Guerrini et al., 2022). PRRT2 is composed of a large proline-rich intracellular NH_2-terminal domain and a COOH-terminal transmembrane (TM) domain composed of two hydrophobic segments of which the first one forms a helix-loop-helix structure within the inner

Abbreviations: BAP, bacterial alkaline phosphatase; DAPI, 4′,6′-diamidino-2-phenylindole; GOF, gain-of-function; HA, human influenza hemagglutinin; Hek293, human embryonic kidney 293; HMR, hydrogen mass repartitioning; J, current density; KO, knockout; LOF, loss-of-function; MD, molecular dynamics; Nav, voltage-dependent sodium channel α-subunit; NKA, Na^+/K^+-ATPase; NMD, nonsense-mediated RNA decay; PBS, phosphate-buffered saline; POPC, 1-palmitoyl-2-oleoyl-*sn*-glycero-3-phosphocholine; PFA, paraformaldehyde; PRRT2, proline-rich transmembrane protein-2; SDS-PAGE, sodium dodecylsulfate gel electrophoresis; TM, transmembrane; WT, wild type.

* Correspondence to: Fabio Benfenati, Center for Synaptic Neuroscience and Technology, Istituto Italiano di Tecnologia, Largo Rosanna Benzi 10, Genova 16132, Italy.
** Correspondence to: Anna Corradi, Department of Experimental Medicine, University of Genova, Viale Benedetto XV, 3, Genova 16132, Italy.
E-mail addresses: fabio.benfenati@iit.it (F. Benfenati), acorradi@unige.it (A. Corradi).
[1] These authors contributed equally to this work

https://doi.org/10.1016/j.nbd.2023.106177
Received 14 April 2023; Received in revised form 16 May 2023; Accepted 27 May 2023
Available online 2 June 2023

leaflet of the membrane and the second one is fully transmembrane (Rossi et al., 2016; Franchi et al., 2023). In nerve terminals, PRRT2 participates in the protein complex including SNARE proteins, synaptotagmins1/2 and P/Q Ca^{2+} channels, increasing the Ca^{2+} sensitivity neurotransmitter release and decreasing synaptic facilitation (Valente et al., 2016, 2019; Coleman et al., 2018; Ferrante et al., 2021). More recently, PRRT2 was demonstrated to inhibit intrinsic neuronal excitability by negatively modulating Nav1.2/1.6 channels (Fruscione et al., 2018; Valente et al., 2019, 2022; Franchi et al., 2023) and enhancing the activity and pump current of Na^+/K^+-ATPase (Sterlini et al., 2021).

PRRT2 came to the attention of neuroscience research being the causative gene for a wide spectrum of neurological disorders with paroxysmal manifestations (Chen et al., 2011; Lee et al., 2012). PRRT2 pathogenic variants account for a large fraction of cases of Benign Familial Infantile Epilepsy (BFIE), Paroxysmal Kinesigenic Dyskinesia (PKD) and Paroxysmal Kinesigenic Dyskinesia with Infantile Convulsions (PKD/IC) and, conversely, 95% of PRRT2 patients have a diagnosis within the BFIE-PKD/IC-PKD spectrum. The remaining PRRT2 patients display other disorders that share the paroxysmal character of the attacks, such as episodic ataxia or hemiplegic migraine (Ebrahimi-Fakhari et al., 2015; Gardiner et al., 2015; Döring et al., 2020; Guerrini et al., 2022). Relatively rare patients characterized by compound heterozygosity or homozygosity present with a severe developmental encephalopathic phenotype with developmental delay and intellectual disability (Labate et al., 2012; Delcourt et al., 2015; Huang et al., 2015). To date, over 130 different mutations have been reported, mostly of familial origin, with over 75% of patients carrying the same frameshift mutation (c.649dupC). The DNA sequence in this "mutational hotspot" is composed by a homopolymer of four guanine bases followed by nine consecutive cytosine bases. This peculiar sequence seems particularly prone to mutations given the frequent duplications, deletions and insertions in the very same cytosine stretch leading to the insertion of a precocious stop codon or generating fully unrelated downstream sequences (Valtorta et al., 2016; Ebrahimi-Fakhari et al., 2015). This results in an unstable mRNA that is eliminated by nonsense-mediated RNA decay (NMD) and/or, in case of NMD escape, to a truncated protein that is degraded (Wu et al., 2014; Liu et al., 2016; Pan et al., 2020). This haploinsufficiency is consistent with a loss-of-function (LOF) mechanism for PRRT2-associated diseases.

The generation of PRRT2 knockout (KO) mice has greatly contributed to the understanding of the pathogenesis of paroxysmal disorders associated with LOF mutations in *PRRT2*. Genetic deletion of the *PRRT2* gene in the mouse (PRRT2-KO) mimics the human pathology with an increased epileptic propensity, complex movement disorders and paroxysmal attacks triggered by sensory stimuli (Michetti et al., 2017a; Tan et al., 2018). PRRT2-KO mouse neurons and iPSC-derived human neurons from homozygous patients display increased Na^+ current densities that are responsible for network hyperexcitability. Such network instability is particularly noticeable in brain areas where PRRT2 is highly expressed, such as the cerebellum and the hippocampus that are responsible for the paroxysmal phenotype of PRRT2-KO mice (Michetti et al., 2017a; Tan et al., 2018; Mo et al., 2019; Calame et al., 2020; Binda et al., 2021; Lu et al., 2021). Interestingly, while PRRT2 is a physiological inhibitor of Nav1.2/Nav1.6 which sustain the firing of excitatory neurons, it does not affect Nav1.1 channels that are fundamental for the excitability of inhibitory neurons (Catterall et al., 2020; Mantegazza et al., 2021), thus generating an excitatory/inhibitory unbalance (Fruscione et al., 2018; Valente et al., 2019). While the increased synaptic facilitation in the absence of PRRT2 can contribute to network hyperexcitability, the dysfunction of Nav channels seems to play a central role in the pathogenesis of PRRT2-linked disorders, as demonstrated by the successful therapeutic control of PRRT2 symptoms by Nav blockers such as carbamazepine or oxcarbazepine, but not by other antiepileptic drugs with different targets (Dale et al., 2014; Chou et al., 2014; Suzuki-Muromoto et al., 2020; Zhao et al., 2021; Döring et al., 2022). PRRT2 negatively modulates Nav1.2/1.6 channels by decreasing their targeting to the plasma membrane, widening the voltage range in which Navs are inactivated and slowing down Nav recovery after inactivation (Fruscione et al., 2018; Valente et al., 2019, 2022). All these biophysical effects are largely opposite to those promoted by Nav β-subunits, of which PRRT2 appears as a physiological, but not molecular, antagonist (Winters and Isom, 2016; Valente et al., 2022).

Besides nonsense variants, about 60 missense mutations of PRRT2 are documented in PRRT2-related disorders (Liu et al., 2016; Tsai et al., 2019; Zhao et al., 2020). Although most of these mutations also cause degradation or decreased targeting to the plasma membrane, some of them display a normal membrane expression and location. The latter ones are particularly interesting for physiological studies, as they can reveal important structure-function relationships and information on the subcellular targeting and downstream interactors of PRRT2. In this respect, two-thirds of the described pathogenic point mutations concentrate in the relatively short (79 amino acids) COOH-terminal domain of PRRT2, characterized by a stable TM configuration (Rossi et al., 2016; Franchi et al., 2023). This observation suggests a crucial role of this domain in the PRRT2 function, as well as in the binding to downstream interactors. Indeed, the COOH-terminal domain of PRRT2 was recently demonstrated to be responsible for the specific regulation of Nav1.2 function (Franchi et al., 2023). However, a very low number of PRRT2 pathogenic variants has been functionally studied thus far (Li et al., 2015; Liu et al., 2016; Coleman et al., 2018).

In this study, we have investigated the impact of a group of 8 missense COOH-terminal mutations of PRRT2 on its structure and interactions with Nav1.2 channels, the likely candidate mediating the pathogenic effects of PRRT2 variants. These pathogenic variants include: the A320V mutant discovered in a family with PKD and BFIE (Lu et al., 2018); the V286M mutant identified in a patient with PKD (Li et al., 2019); the recently described de novo heterozygous missense mutation V319L in exon 3 of the gene (Fang et al., 2020); the recently discovered mutant I270V with a still unknown effect on PRRT2 expression (Balagura et al., 2020); four mutants (R266W, R308C, R311W, I327M) that were previously demonstrated to be expressed and membrane-targeted in heterologous systems (Zhao et al., 2020). We found that the A320V and V286M mutants have a clear phenotype on the PRRT2-Nav1.2 functional interactions with the former characterized by LOF and the latter by an unexpected gain-of-function (GOF) with respect to wild-type PRRT2 (WT-PRRT2). The data confirm the key role played by Nav channel dysregulation in the pathogenesis of PRRT2-linked disorders and suggest that circuit instability and paroxysmal manifestations may arise when PRRT2 activity exits its physiological range.

2. Materials and methods

2.1. Constructs and mutagenesis

The used plasmids are: PRRT2-HA: pKH3-*PRRT2*-HA vector encoding for the human PRRT2 cDNA tagged at COOH-terminal with the 3xHA epitope (Rossi et al., 2016); BAP-HA: pKH3-*BAP*-HA vector encoding for Bacterial Alkaline Phosphatase with HA tags fused at C terminus. The pKH3-PRRT2-HA vector was used as template to obtain mutant PRRT2 isoforms by site-directed mutagenesis using the QuikChange Lightning site-directed mutagenesis kit (Agilent). The used forward primers are:

R266W - GTGAAGGCACCCAGAAACCTTGGGACTACATCATC;
I270N – CTCGGGACTACATCAACCTTGCCATCCTGTC;
V286M – GTGGCCTGTCAACATCATGGCCTTCGCTTATGC;
R308C – GTGGACGGGGCCCAGTGTCTGGGCCGGGTAG;
R311W – GGCCCAGCGTCTGGGCTGGGTAGCCAAGCTCTTAAGC;
V319L – CAAGCTCTTAAGCATCTTGGCGCTGGTGGG;
A320V – CTCTTAAGCATCGTGGTGCTGGTGGGGGGA;
I327M – GGGGAGTCCTCATGATCATCGCCTCCTGC.

All primers were purchased from Eurofins Genomics (Ebersberg,

Germany).

2.2. Cell culture and transfection

Hek293 cells stably expressing human Nav1.2 were kind gifts from Drs. Enzo Wanke and Marzia Lecchi (Milano-Bicocca University, Italy). All Hek293 cell lines were maintained in DMEM/F12 (1:1) supplemented with 10% fetal bovine serum, 100 U/ml penicillin, 100 μg/ml streptomycin and, for selection of stable Nav clones, 500 μg/ml G418. Cell lines were transfected with 2 μg of each plasmid according to the manufacturer's recommendations at 70% confluency using Lipofectamine 2000 (Life Technologies). All reagents were purchased from ThermoFisher Scientific. To identify transfected cells for electrophysiology, the reporter EGFP or Tomato protein reporter (Clontech) was co-transfected. For electrophysiological experiments, transfected cells were dissociated, re-plated at low density about 24 h post-transfection and recorded after further 24 h. To study the effect of PRRT2 pathogenetic mutants, Hek293/Nav1.2 were transfected with the MOCK, WT-PRRT2, A320V-PRRT2 or V286M-PRRT2 tagged with HA.

2.3. SDS-PAGE and Western blotting

For sodium dodecylsulfate gel electrophoresis (SDS-PAGE), samples were quantified with the BCA assay (ThermoFisher Scientific) and heated to 50 °C for 5 min without boiling and successively run on 10% (*w/v*) polyacrylamide gels and blotted onto nitrocellulose membranes (Whatman). Blotted membranes were blocked for 1 h in 5% milk in Tris-buffered saline (10 mM Tris, 150 mM NaCl, pH 8.0) plus 0.1% Triton X-100 and incubated overnight at 4 °C with the appropriate primary antibody. Membranes were washed and incubated at room temperature for 1 h with peroxidase-conjugated anti-mouse (Cat.#1706516; 1:3000; BioRad, Hercules, CA) or anti-rabbit (Cat.#1706515; 1:3000; BioRad, Hercules, CA) antibodies. Bands were revealed with the ECL chemiluminescence detection system (ThermoFisher Scientific) and imaged by the ChemiDoc Imaging System (Bio-Rad). Immunoblots were quantified by densitometric analysis of the fluorograms (Quantity One software; Bio-Rad, Hercules, CA) obtained in the linear range of the emulsion response.

2.4. Pull down and surface biotinylation assays

Naïve Hek293 cells were transfected as previously described with HA-tagged WT-PRRT2 and its mutant isoforms, using HA-tagged bacterial alkaline phosphatase (BAP-HA) as control. Both protocols were performed at 4 °C. For pull-down assays, 24 h after transfection, cells were harvested in lysis buffer (150 mM NaCl, 50 mM Tris, 1 mM EDTA and 1% Triton X-100 supplemented with protease inhibitor cocktail) and centrifuged at 10,000 x*g* for 10 min. Kept an aliquot for the input sample, the supernatant was incubated with 50 μl of monoclonal anti-HA-agarose affinity beads (Sigma-Aldrich) for 2 h. After 3 washes in lysis buffer, beads were incubated with cell extracts from Hek293 cells stably expressing Nav1.2 for 3 h. After extensive washes in lysis buffer and detergent-free lysis buffer, samples were resolved by SDS-PAGE and subjected to western blotting with anti-panNav (Cat.#s8809; 1:300; Sigma-Aldrich) and anti-HA (Cat.# 71–5500; 1:1,000; ThermoFisher Scientific) specific antibodies.

For biotinylation experiments, Hek293 cells stably expressing Nav1.2 were transfected with either WT-PRRT2 or its variants tagged with HA. Twenty-four hours after transfection, cells were incubated with 1 mg/ml of EZ-Link™ Sulfo-NHS-SS-Biotin (ThermoFisher Scientific) in cold phosphate buffered saline (PBS, pH 8) for 35 min, with constant mixing. Free biotin was quenched, twice with 100 mM Tris pH 8, and once with cold PBS to remove the excess of biotin. Cells were then lysed in lysis buffer (150 mM NaCl, 50 mM Tris, 1 mM EDTA and 1% Triton X-100) supplemented with protease inhibitor cocktail (Cell Signaling). Total cell lysates were centrifuged at 10,000 x*g* for 10 min. Kept an aliquot for the input sample, the supernatant fraction was incubated with 150 μl of NeutrAvidin conjugated agarose beads (ThermoFisher Scientific) at 4 °C for 3 h. After extensive washes of the beads, samples were eluted, resolved by SDS-PAGE and subjected to western blotting with anti-panNav (Cat.# s8809; 1:300; Sigma-Aldrich), anti-NKA 1 (Cat.# 05–369; 1:1,000; Merck), anti-Actin (Cat.# A4700; 1:1,000; Sigma Aldrich) or HA (Cat.# 71–5500; 1:1,000; ThermoFisher Scientific) antibodies.

2.5. Live cell immunolabeling

Naïve Hek293 cells transfected with PRRT2 mutant isoforms constructs were maintained for 10 min at 4 °C, and then were live labelled by incubation with primary anti-HA rabbit antibody (Cat.# 71–5500; 1:500; ThermoFisherScientific, 1:500 diluted in culture medium) for 20 min at 4 °C to detect surface epitopes. Samples were incubated with the secondary antibody Alexa Fluor 488 for 20 min at 4 °C and then were fixed by 4% paraformaldehyde (PFA) for 20 min at room temperature. After several washes in PBS, coverslips were mounted using Prolong Gold antifade reagent (Invitrogen) containing 4′,6′-diamidino-2-phenylindole (DAPI) for nuclear staining.

2.6. Electrophysiological recordings

Patch pipettes, prepared from thin-borosilicate glass (Hilgenberg) were pulled and fire-polished to a final resistance of 2–4 MΩ when filled with standard internal solution. Whole-cell currents were recorded using an EPC-10 amplifier (HEKA Electronic). Recordings with leak currents >200 pA or series resistance >10 MΩ were discarded. Linear capacity and leakage currents were eliminated by P/N leak subtraction procedure. For all electrophysiological experiments data acquisition was performed using PatchMaster programs (HEKA Elektronic) as described previously (Fruscione et al., 2018; Valente et al., 2022; Franchi et al., 2023). Series resistance was compensated 80% (2 μs response time) and the compensation was readjusted before each stimulation. All recordings were performed at 22–24 °C. Voltage-clamp recordings of voltage-gated Na^+ currents were performed using the following solutions: extracellular (in mM): 140 NaCl, 3 KCl, 1 $MgCl_2$, 1 $CaCl_2$, 10 HEPES, 10 mannitol (pH 7.3 with NaOH); intracellular (in mM): 140 CsCl, 10 NaCl, 2 EGTA, 10 HEPES (pH 7.3 with CsOH). For the experiments with the pathogenic variants, whole-cell family currents of fast inactivating Nav channels were evoked by 5 mV steps depolarization from −80 to 40 mV and cells were held at −100 mV.

Steady-state inactivation curves were constructed by recording the peak currents amplitude evoked by 20-ms test pulses to −10 mV after 500-ms pre-pulses to potentials over the range of −130 to 20 mV. Time-dependent rate of recovery from inactivation was calculated by pre-pulsing the cell with a 20-ms step to −20 mV to inactivate Na^+ channels and then bringing back the potential to −100 mV for increasing recovery durations (0.5, 1, 2, 4, 8, 32, 64, 128, 256 ms) before the test pulse of −mV. Time constants for recovery from inactivation were calculated by fitting data from each recorded cell using a two-exponential function and averaging time constants across cells. To investigate the frequency-dependent inhibition, a series of depolarizing pulses to +10 mV from a holding potential of −100 mV for 12 ms at a frequency of 20 Hz was applied (Merrick et al., 2010). Peak current was normalized to the first pulse in each experiment.

The Na^+ current density (J) was obtained by dividing the peak inward current by the cell capacitance (nA/pF). The conductance/voltage relationship (G-V) curves were obtained by converting the maximal current values, evoked with the voltage step protocols, to conductance using the relation $G_{Na} = I_{Na}/(V\text{-}E_{Na})$, where G_{Na} is the Na^+ conductance, I_{Na} is the peak Na^+ current, V is the command pulse potential, and E_{Na} is the theoretical reversal potential of Na^+ current calculated by Nernst eq. G-V curves were normalized and fitted with the Boltzmann function $G/G_{max} = 1 / (1 + \exp. [(V - V_{1/2})/k]$, where G is the conductance, G_{max} is

the maximal conductance, $V_{1/2}$ is the half-maximal voltage of activation, and k is the slope factor. Inactivation curves were fitted with the Boltzmann equation in the following form: $1 / [1 + \exp. (V_{1/2} - V)/k]$. To minimize space-clamp problems, we recoded only isolated transfected cells with a soma diameter of about <30 μm.

2.7. Molecular dynamics simulations

Molecular dynamics (MD) simulations were performed using NAMD3.0alpha6 (Phillips et al., 2020) with the CHARMM36m force field, a refined version of the all-atom additive CHARMM36 protein force field (Brooks et al., 2009; Huang et al., 2017). The membrane builder application of the CHARMM-GUI server (Jo et al., 2008; Lee et al., 2016) was used to insert single point mutations for missense pathogenetic isoforms of WT-PRRT2 protein, introduced in Fig. 1 and for the preparation of all the inputs used during the simulations. For each run, the protein transmembrane domain (G261 to K340 of the human PRRT2 sequence) was pre-oriented using PPM server (Lomize et al., 2012) and inserted into a pre-equilibrated 1-palmitoyl-2-oleoyl-*sn*-glycero-3-phosphocholine (POPC) lipid bilayer. TIP3P water model (Neria et al., 1996) was used for solvation while NaCl ions were added to neutralize the total system charge at a physiological concentration of 0.15 M. The whole system counted ~110,000 atoms in a rectangular box [110x110x97 $Å^3$].

Periodic boundary conditions were applied to replicate the system and remove box surface effects, and the particle mesh Ewald method was used for long-range electrostatics (Darden et al., 1993), with a grid spacing of 1 Å and sixth-order B-splines. A cutoff of 12 Å and smooth

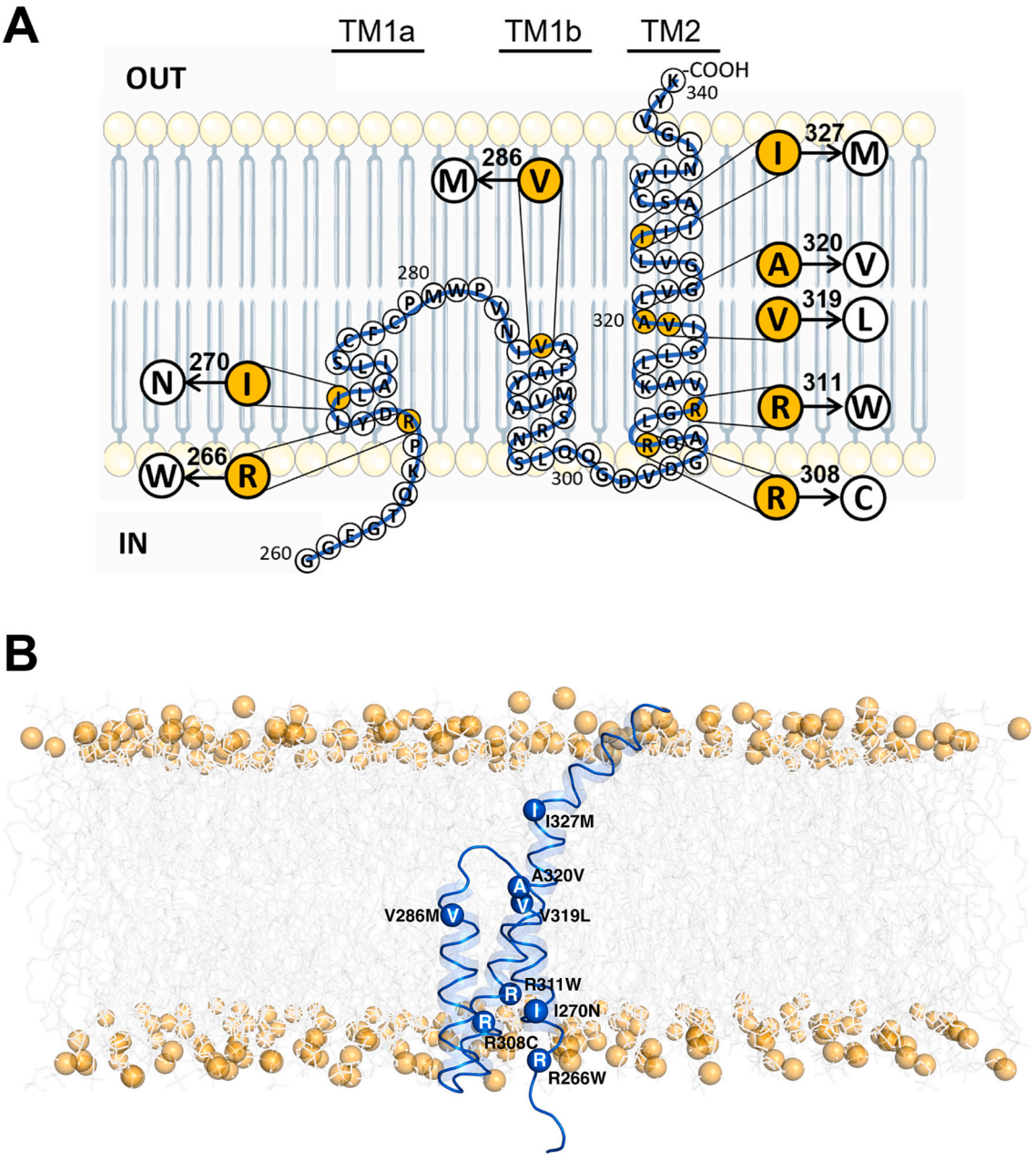

Fig. 1. Multidimensional maps of missense mutations within the PRRT2 membrane-associated domain.
A. Schematic 2D view of the PRRT2 TM domain. The eight PRRT2 missense pathogenic variants investigated in this study are highlighted. B. Snapshot of the TM domain of PRRT2 extracted from an MD trajectory. The backbone of the protein is represented as a blue transparent ribbon; α-carbons of mutated residues are shown as navy blue spheres; phospholipid acyl tails are depicted as transparent grey sticks; phosphate atoms are shown as orange spheres. Water molecules are not included for clarity. (For interpretation of the references to colour in this figure legend, the reader is referred to the web version of this article.)

switching at 10 Å was used for Lennard-Jones interactions. Chemical bond distances involving hydrogen atoms were constrained using the SHAKE/RATTLE algorithm (Andersen, 1983). The systems were energy minimized and further equilibrated by running 13-ns NPT simulation using positional restraints on the proteins atoms with $P = 1$ atm and $T = 310$ K, maintained by a Langevin thermostat and Nosé-Hoover Langevin piston pressure control (Feller et al., 1995). Subsequently, eight MD simulations were generated in the NPT ensemble, each 1 μs long, at the same temperature and pressure used in the equilibration stage. Hydrogen Mass Repartitioning (HMR) (Hopkins et al., 2015; Balusek et al., 2019) was used for all the systems, allowing for a time-step of 4 fs. The MD trajectories were analyzed using VMD (Humphrey et al., 1996) and PyMOL (The PyMOL Molecular Graphics System, Version 2.0 Schrödinger, LLC).

2.8. Statistical analysis

Experimental data are expressed as either bar plots with superimposed individual experimental points corresponding to the number of independent preparations or box plots characterized by the following elements: centre line, median (Q2); box limits, 25th (Q1)-75th (Q3) percentiles; whiskers, min to max values. Normal distribution of data was assessed using the D'Agostino-Pearson's normality test. To compare more than two normally distributed sample groups, one-way ANOVA, followed by post hoc multiple comparison tests was used. In cases in which data were not normally distributed, non-parametric one-way ANOVA (Kruskal-Wallis' test) followed by the Dunn's multiple comparison test was used. Alpha levels for all tests were 0.05% (95% confidence intervals). Statistical analysis was carried out using the Prism (GraphPad Software, Inc.) software.

3. Results

Sixty missense mutants have been reported so far (Table 1; Fig. S1), the majority of which (Tsai et al., 2019) is concentrated in the COOH-terminal TM domain of PRRT2 implicated in the modulation of Nav1.2/1.6 channels. We focused on a restricted number of COOH-terminal missense pathogenic variants (Fig. 1) and studied their impact on the modulation of PRRT2/Nav1.2 interaction to unravel possible pathogenic mechanisms. To this aim, we chose 4 mutants that were already reported to be expressed in heterologous systems (R266W, R308C, R311W, I327M; Zhao et al., 2020), plus 4 further point mutations (I270N, V286M, V319L, A320V) that were not previously investigated.

3.1. The PRRT2 missense mutants display physiological expression levels and membrane targeting

Pathogenic PRRT2 mutants were generated by site-directed mutagenesis in the pKH3-PRRT2-HA vector encoding for the human PRRT2 cDNA tagged at COOH-terminal with the 3xHA epitope (Rossi et al., 2016). Before proceeding with further functional studies, it was important to verify that the expression of these variants and their membrane localization were not altered with respect to WT-PRRT2. Western blot analysis of PRRT2 mutants transfected in the naïve Hek293 cell line (Fig. 2A, left) revealed that the expression of all mutants was only slightly decreased with respect to WT-PRRT2, although none of these differences approached statistical significance (Fig. 2A, right).

Missense mutations are often causative of PRRT2 mislocalization and altered trafficking to the plasma membrane. Thus, we investigated the membrane expression of the mutant isoforms by immunofluorescence on live cells, taking advantage of the extracellular HA epitopes fused at the COOH-terminus of PRRT2. Transfected cells were imaged by confocal microscopy (Fig. 2B, left), and the surface fluorescent signals were normalized to the respective transfection efficiency. Interestingly, all studied variants preserved a correct targeting to the membrane similar to WT-PRRT2 (Fig. 2B, right). We conclude that the missense mutations analyzed do not significantly affect protein expression and membrane localization and thereby can be subjected to the functional study of the interactions with Nav channels.

3.2. PRRT2 missense variants do not impact on the structural stability of the membrane-associated domain

We investigated how the pathogenic variants shown in Fig. 1 affect the conformation of PRRT2 TM domain. In lack of an experimentally derived structure, we previously generated an all-atom model of the native protein domain (residues G261-K340), and we thoroughly refined it in a membrane-water environment using molecular dynamics (MD) simulations (Rossi et al., 2016; Franchi et al., 2023). Here, we performed eight independent, 1 μs-long MD simulations of the PRRT2 mutants using the HMR protocol already employed for the WT simulations (Franchi et al., 2023). In all cases, we observed that the protein structure remains stable: the **α**-carbon RMSDs of all systems are stationary after 300 ns (Fig. 3), and the time evolution of cross-distances between residues A272, S294 and A313, localized at the core of the intramembrane helices, does not display major drifts (Figs. S2 and S3). According to these results, the mutations do not alter the integrity of the PRRT2 fold, despite their distinct locations along the protein sequence.

3.3. The V286M and A320V variants have opposite effects on the interaction between PRRT2 and Nav1.2

Since the mutations analyzed do not alter either the PRRT2 expression or the stability of the membrane-associated domain that regulates the Nav/PRRT2 interaction, we next studied whether they could affect the binding between PRRT2 and Nav1.2 channels. Pull-down

Table 1
List of the selected missense pathogenic variants in the PRRT2 membrane-associated domain and their phenotypic characterization.

PRRT2 variant		Phenotype	Poly-phen2	Protein expression	Plasma membrane targeting	References
c.796C > T	R266W	PKD	Probably damaging/ damaging	Expression similar to WT (100%)	Expression similar to WT (100%)	Zhao et al., 2020
c.809T > A	I270N	PKD	Unknow	Unknown	Unknown	Balagura et al., 2020
c.856G > A	V286M	PKD	Probably damaging	Unknown	Unknown	Li et al., 2019
c.922C > T	R308C	PKD	Probably damaging/ damaging	Expression 50% of WT	Expression 50% of WT	Zhao et al., 2020, Tsai et al., 2019
c.931C > T	R311W	PKD, EA	Probably damaging	Expression similar to WT (100%)	Expression similar to WT (100%)	Zhao et al., 2020, Tsai et al., 2019
c.955G > T	V319L	PKD	Probably damaging	Unknown	Unknown	Fang et al., 2020
c.959C > T	A320V	PKD, BFIE	Probably damaging	Unknown	Unknown	Lu et al., 2018
c.981C > G	I327M	PKD, BFIE	Probably damaging/ damaging	Expression similar to WT (100%)	Expression similar to WT (100%)	Zhao et al., 2020, Tsai et al., 2019

PKD, paroxysmal kinesigenic dyskinesia; EA, episodic ataxia; BFIE, benign familial infantile epilepsy; WT, wild type.

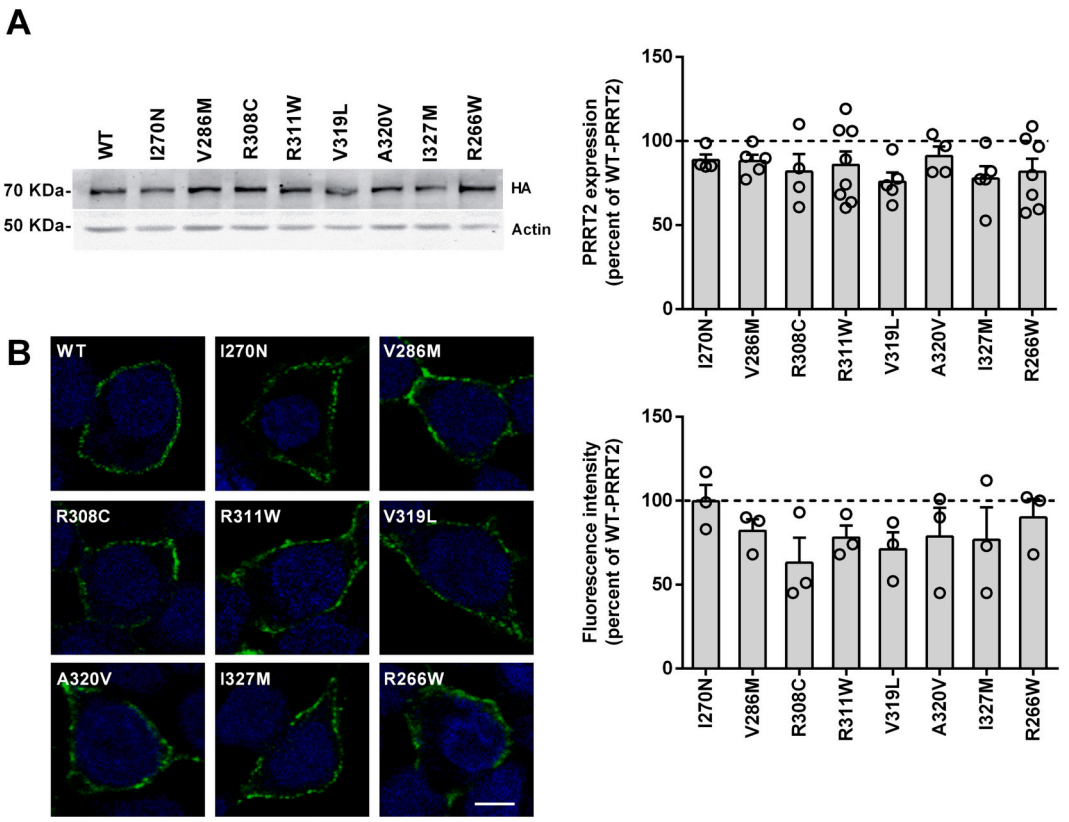

Fig. 2. Expression levels and membrane targeting of missense PRRT2 mutants.
A. Protein extracts from naïve Hek293 cells transfected with either WT or mutant PRRT2-HA variants were analyzed by western blotting using anti-HA antibodies. *Left:* Representative immunoblot. *Right:* Densitometric analysis of the immunoreactive bands. Actin was used as loading control. The expression levels of PRRT2 mutants are shown in percent of the immunoreactivity of WT-PRRT2 as means ± sem of $n = 4$–8 independent experiments (horizontal line; mean ± sem: 100 ± 0.49). B. *Left:* Representative confocal images of naïve Hek293 cells transfected with either WT or mutant PRRT2-HA variants and live surface-immunolabelled with anti-HA antibodies (green). DAPI staining (blue) was used to visualize nuclei. Scale bar, 5 μm. *Right:* Quantification of HA fluorescence intensity. Fluorescence intensity was calculated as the ratio between the total HA fluorescence signal and the transfection efficiency in the same field and expressed in percent of WT-PRRT2 (horizontal line). Data represent means ± sem with superimposed individual values from $n = 3$ independent experiments. Statistical analysis was done using one-way ANOVA/Holm-Šídák tests. (For interpretation of the references to colour in this figure legend, the reader is referred to the web version of this article.)

experiments were performed to investigate whether the PRRT2 mutants could bind the Nav1.2 channel with the same efficiency as WT-PRRT2. Since co-expression of PRRT2 in Nav-stably transfected Hek293 may result in different expression levels of the two interactors, we separately expressed HA-tagged PRRT2 variants in naïve Hek293 and affinity purified them therefrom. Then, we set on-bead binding assays by challenging PRRT2-HA isoforms with extracts of Hek293 cells stably expressing the Nav1.2 channel α-subunit (Hek-Nav1.2). An additional construct, encoding for the unrelated protein BAP, also tagged with HA, was used as a negative control. PRRT2 variants were pulled down and the bound Nav1.2 channels detected by western blotting with anti-panNav antibodies (Fig. 4A). While 6 of the 8 mutants displayed a Nav1.2 binding similar to WT-PRRT2, the A320V and V286M mutants showed a significant alteration in their binding to the channel (Fig. 4B). In particular, V286M pulled down a higher amount of Nav1.2, suggesting a binding higher than WT-PRRT2, while the isoform A320V immunoprecipitated a smaller amount of the channel. The altered Nav1.2 binding of PRRT2 mutants may cause channel dysregulation and contribute to the onset of PRRT2-related pathologies.

3.4. The PRRT2 A320V mutant increases the surface exposure of Nav1.2 channels

Since PRRT2 interaction with Nav1.2/Nav1.6 channels modulates their plasma membrane expression (Fruscione et al., 2018), we investigated whether the altered binding of the A320V and V286M mutants affects membrane targeting of Nav1.2. To this end, we performed biotinylation experiments in Hek-Nav1.2 cells transfected with either WT-PRRT2 or its variants and measured the amount of Nav1.2 expressed in the membrane biotinylated protein fraction. In addition to the A320V and V286M, two additional mutants characterized by unchanged Nav1.2 binding (I270N and V319L) were tested as controls in addition to WT-PRRT2. The results showed that the A320V mutant increases the membrane expression levels of Nav1.2 compared to WT-PRRT2, suggesting that this mutant lack the ability to negatively regulate the Nav1.2 membrane exposure (Fig. 5). No significant differences in Nav channels exposure were found for the I270N, V286M and V319L variants.

3.5. The PRRT2 V286M and A320V mutants have opposite effects on the steady-state inactivation kinetics of Nav1.2 channels

Given the above results, we investigated in detail the functional effects of the altered interaction of the A320V and V286M mutants with Nav1.2 channels by patch-clamp electrophysiology of Hek-Nav1.2 transiently transfected with either variant (Fig. 6A). Consistent with the biotinylation studies, the A320V mutant was significantly less effective than WT-PRRT2 in downregulating transient macroscopic Na^+ currents, and not significantly different from MOCK-transfected cells. On the other hand, the V286M mutant was still able to significantly decrease Na^+ conductance with respect to MOCK-transfected cells, and its effect was not significantly different from WT-PRRT2 (Fig. 6B,C).

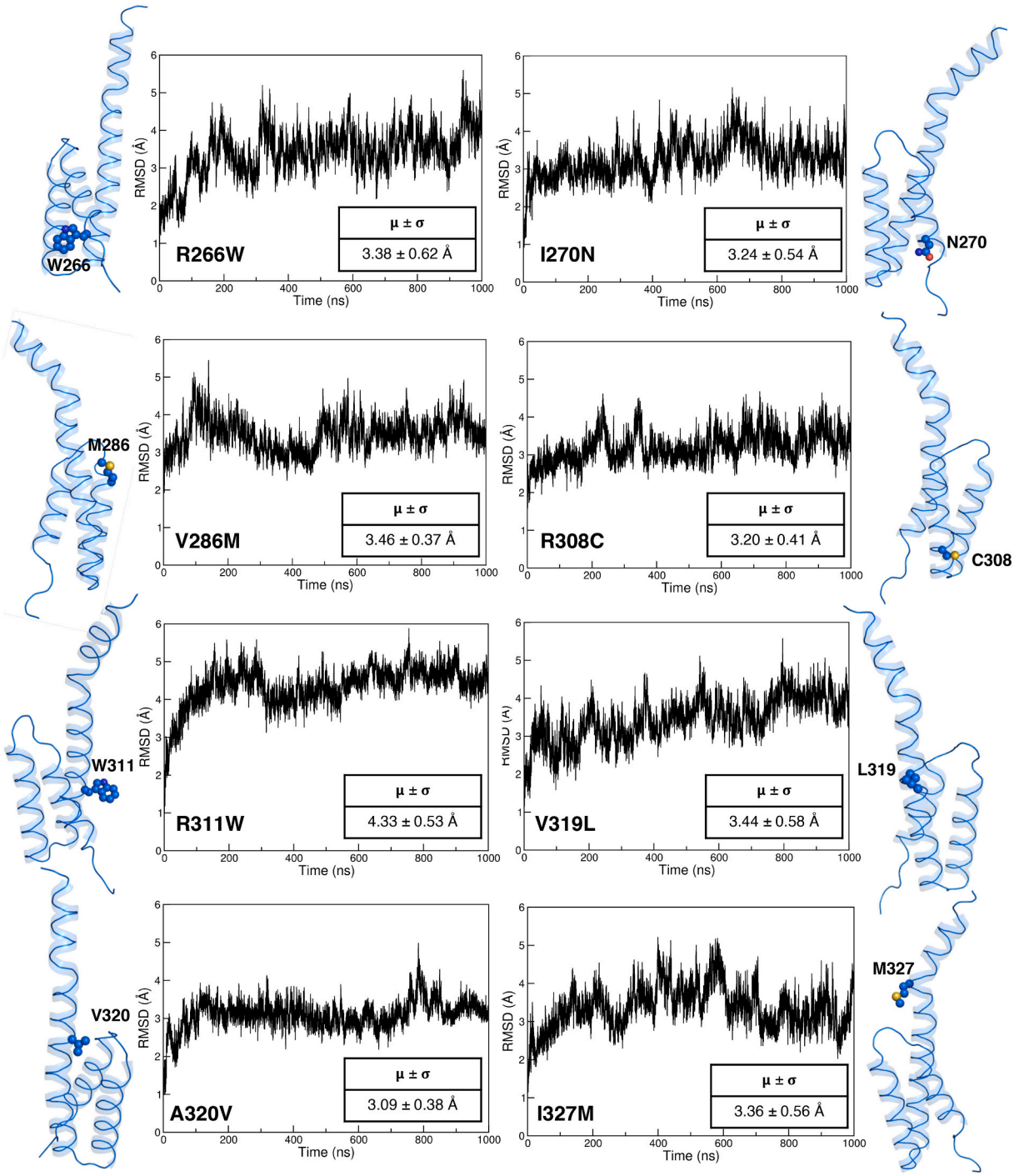

Fig. 3. Structural stability assessment for PRRT2 modelled mutants by Molecular Dynamics simulations.
Time-evolution of the **α**-carbon RMSDs in the mutant simulations, with average values (μ) reported. The mutated spots are highlighted as spheres in the structural models shown for each system.

Being unaffected by WT-PRRT2 (Fruscione et al., 2018), the activation dynamics of Nav1.2 was not modified by either PRRT2 mutant (Fig. 6D, E).

The analysis of the Nav1.2 inactivation kinetics confirmed the previously reported left-shift of the steady-state inactivation curve by WT-PRRT2 with respect to MOCK-transfected cells. Interestingly, the magnitude of this effect was increased by the V286M mutant, with a significant additional left shift of the inactivation curve (GOF), while the PRRT2 effect was lost with the A320V mutant that became similar to MOCK-transfected cells (LOF) (Fig. 6F,G).

3.6. The A320V and V286M PRRT2 mutants have opposite effects on the recovery from inactivation of Nav1.2 channels

We previously reported that WT-PRRT2 slows down and decreases the magnitude of the recovery from inactivation of Nav1.2/1.6 channels (Fruscione et al., 2018; Valente et al., 2022). Interestingly, the PRRT2-mediated inhibition of Nav1.2 recovery was totally lost with the A320V mutant, confirming its LOF phenotype and suggesting a key role for this PRRT2 residue in the modulation of the biophysical properties of the Nav1.2 channel (Fig. 7A,B). In contrast, the V286M mutant

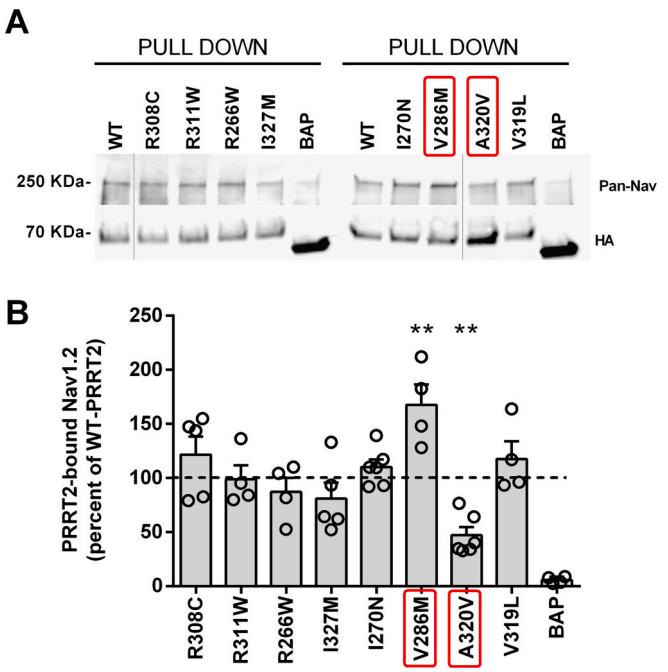

Fig. 4. Binding of missense PRRT2 mutants to Nav1.2 channels.
The binding ability of PRRT2 mutants to the Nav1.2 channel was analyzed by pull down assays. A. Naïve Hek293 cells were transfected with HA-tagged WT-PRRT2, mutant PRRT2 variants or the control unrelated protein BAP, extracted and immunoprecipitated using anti-HA beads. HA-bound proteins were subsequently incubated with lysates of Nav1.2-expressing Hek293 stable cell clones. HA-pulled-down samples were analyzed by western blotting using anti-panNav antibodies. Representative immunoblots are shown. Vertical grey lines in the blots indicate that the lanes were on the same gel but have been repositioned. B. Quantification of the panNav immunoreactivity in PRRT2 immunoprecipitates. Immunoblots were analyzed by densitometry of the fluorograms. The intensity of Nav1.2 immunoreactivity was normalized to the PRRT2 recovery within the same sample. The binding of PRRT2 mutants to Nav1.2 is expressed in percent of WT-PRRT2 (horizontal line; mean ± sem: 100 ± 8.27). Red boxes indicate the PRRT2 variants that showed altered Nav1.2 binding and were subjected to further analysis. Data represent means ± sem with superimposed individual values from n = 4–6 independent experiments. $^{**}p < 0.01$, one-way ANOVA/Holm-Šídák tests. (For interpretation of the references to colour in this figure legend, the reader is referred to the web version of this article.)

confirmed the GOF observed on the inactivation kinetics by showing a decrease in the plateau recovery of the same extent of WT-PRRT2, but characterized by slower kinetics with a two-fold significant increase in the time constant (Fig. 7A,B).

Since WT-PRRT2 anticipates the entry of Nav1.2 channels in the inactivated state and reduces their recovery from inactivation (Fig. 6F and Fig. 7A), it is likely that, during high-frequency stimulation, a progressive increase in Nav1.2 inactivation occurs in the presence of PRRT2. To determine the effects of PRRT2 and its mutants in accumulating inactivated channels, a series of depolarizing pulses from a holding potential of −100 mV to 10 mV at a frequency of 20 Hz were applied (Fig. 7C), as previously described (Merrick et al., 2010). In Hek-Nav1.2 cells expressing WT-PRRT2, stimulation at 20 Hz induced a progressive and significant reduction of Na^+ current amplitude with respect to MOCK-transfected cells, consistent with an increased proportion of inactivated Nav1.2 channels (Fig. 7D). In this context, the A320V mutant induced a significantly slower and reduced depression of the current, confirming its LOF phenotype, while the V286M mutant accelerated the depression in current amplitude due to frequency inhibition with respect to WT-PRRT2 (GOF), while reaching a similar inhibition plateau (Fig. 7D,E).

4. Discussion

The disease mechanisms for paroxysmal disorders associated with nonsense/frameshift mutations in the *PRRT2* gene are largely dependent on the LOF of the mutated allele product due to degradation of either the mRNA by NMD or the truncated protein which has escaped NMD (Wu et al., 2014; Liu et al., 2016; Pan et al., 2020). The few pathogenic missense PRRT2 mutants that are expressed to some extent display lack of membrane targeting of the mutant protein, thus conforming to a general LOF pathogenetic mechanism (Liu et al., 2016; Tsai et al., 2019; Zhao et al., 2020). On the other hand, a few missense pathogenic variants do not greatly affect protein expression and membrane targeting of PRRT2. In this case, the pathogenic mechanism can be more difficult to identify, depending on the potential disruption of interactions of PRRT2 with downstream cellular effectors. The investigation of these mutants can provide useful hints for understanding the structure-function relationships and the functional role of single residues and specific protein regions, as well as for identifying potential new target for therapeutic strategies.

One interesting observation regards the molecular distribution of the PRRT2 missense pathogenic variants that are largely concentrated in the short and highly conserved COOH-terminal domain of the protein. This focuses the attention on the functional importance of the PRRT2 TM domain implicated in regulating fundamental membrane effectors such as voltage-dependent Na^+ channels. This 79-amino acid long TM domain has a stable 3D structure defined by 1-μs MD simulations, confirmed by AlphaFold2 and ESMFold algorithms (Jumper et al., 2021; Rives et al., 2021), and formed by a helix-loop-helix (TM1a/TM1b), a very short cytosolic loop, and a membrane-spanning segment (TM2) ending with a COOH-terminal tripeptide (Fig. 1; Rossi et al., 2016; Franchi et al., 2023). We have recently shown that the COOH-terminal region of PRRT2 could recapitulate the effects of the full-length protein on both current density (a functional measure of the membrane targeting), inactivation kinetics and recovery from inactivation of the Nav1.2 channel (Franchi et al., 2023). Thus, to understand the pathogenesis of the paroxysmal disorders related to PRRT2 point mutations, it is crucial to define whether the mutation has an impact on the physiological regulation of Nav channels by PRRT2. However, virtually all missense PRRT2 mutants investigated thus far were screened only for their expression level and membrane targeting (Liu et al., 2016; Tsai et al., 2019; Zhao et al., 2020).

In this paper, we analyzed an array of missense pathogenic variants targeting the PRRT2 TM domain (4 mutants already reported to be expressed in heterologous systems and 4 point-mutations that were not previously analyzed) and investigated the effects on their downstream effector Nav1.2 in terms of binding, membrane targeting and biophysical properties. Notably, all the considered mutated residues (R266, I270, V286, R308, R311, V319, A320 and I327) are fully conserved across mammalian species, testifying their important structural/functional role within the COOH-terminal domain of PRRT2. The study resulted in the identification of two residues that significantly alter the interactions of PRRT2 with the Nav1.2 channel (Table 2). The V286M and A320V mutants showed an altered binding to Nav1.2 in pull-down experiments, with V286M showing increased and A320V showing decreased binding to Nav1.2, respectively. From a functional point of view, the A320V mutant was characterized by a clear LOF phenotype in both the membrane targeting and biophysical properties of Nav1.2 channels. On the other hand, the V286M mutant showed a GOF phenotype with respect to WT-PRRT2 in the modulation of the Nav1.2 biophysical properties (steady-state inactivation and recovery from inactivation), while it did not significantly affect the membrane targeting of the channel. In spite of the fact that Nav α-subunit-expressing Hek293 cells are very different from neurons in terms of subcompartment trafficking of the channel and absence of auxiliary subunits, the distinct phenotypes of the two mutants suggest that the inhibition of the membrane exposure of Nav1.2 channels and the

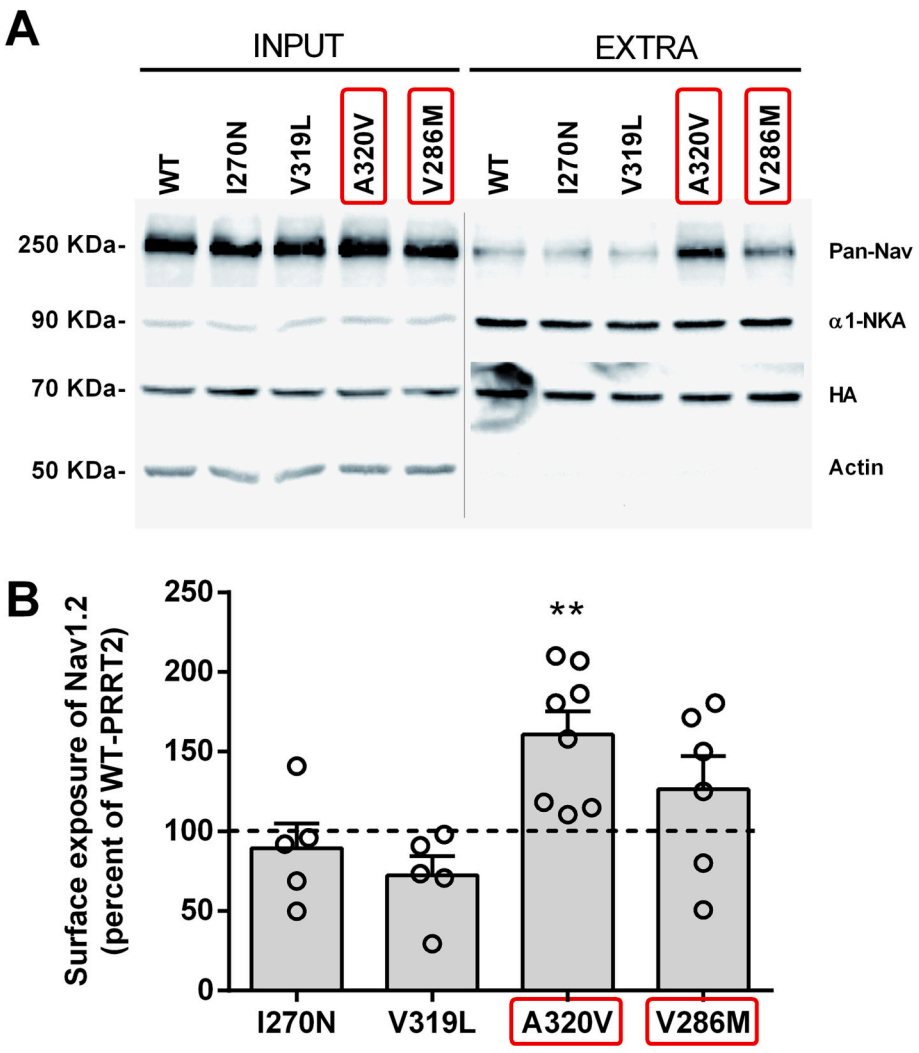

Fig. 5. Effects of missense PRRT2 mutants on the surface exposure of Nav1.2 channels.
A. Representative immunoblots of biotinylation assays. Hek293 cells stably expressing Nav1.2 channels were transfected with either WT or mutant PRRT2-HA variants. Total lysates (INPUT) and biotinylated (cell surface, EXTRA) fractions were analyzed by western blotting with antibodies to HA and panNav. Na^+/K^+-ATPase α1-subunit (α1-NKA) and actin were used as markers of cell surface and intracellular fractions, respectively. Vertical grey lines in the blots indicate that the lanes were on the same gel but have been repositioned. B. Quantification of Nav1.2 surface exposure after normalization to α1-NKA. Data are expressed in percent of the respective WT-PRRT2 values (horizontal line; mean ± sem: 100 ± 5.04). Red boxes indicate the PRRT2 variants with altered Nav1.2 binding that were subjected to electrophysiological analysis. Data represent means ± sem with superimposed individual values from $n = 5–8$ independent experiments. **$p < 0.01$; one-way ANOVA/Holm-Šídák tests. (For interpretation of the references to colour in this figure legend, the reader is referred to the web version of this article.)

modulation of their inactivation kinetics/recovery from inactivation may involve distinct residues of the TM region of PRRT2.

The A320V pathogenic variant in the TM2 region was discovered in a family with PKD and BFIE (Lu et al., 2018). Supported by the very high evolutionary conservation, our results indicate that A320 is an important site for the interaction with the Nav1.2 channel, as its mutation markedly decreases virtually all the physiological effects of PRRT2. In the presence of A320V, PRRT2 loses its inhibitory constraint on the membrane exposure of Nav1.2, offering a likely pathogenetic mechanism for this mutation. As far as the V286M mutant located in the TM1b region is concerned, a pathogenetic mechanism based on the observed GOF activity on Nav1.2 channels is apparently less consistent with the current knowledge of PRRT2 being a network stability gene (Valente et al., 2019; Michetti et al., 2017a, 2017b; Lerche, 2018; Binda et al., 2021; Lu et al., 2021). However, it has very recently been reported that overexpression of PRRT2 in the mouse model of 16p11.2 duplication, which in humans is associated with ASD, epilepsy and intellectual disability, causes hypersynchronous activity, increased glutamate release and seizure propensity (Forrest et al., 2023). It is therefore possible that both insufficient or excessive levels of PRRT2, and thereby LOF or GOF PRRT2 mutants, are detrimental to the stability of neuronal networks and cause paroxysmal manifestations. However, in the present study, the PRRT2 mutants were investigated only for their Nav1.2 interaction activity, and the possibility exists that they also alter PRRT2 activities at the presynaptic level (Valente et al., 2016; Valente et al., 2019; Michetti et al., 2017a; Coleman et al., 2018) or on other effectors such as voltage-gated Ca^{2+} channels or Na^+/K^+-ATPase (Ferrante et al., 2021; Sterlini et al., 2021).

In conclusion, we screened a cohort of 8 PRRT2 missense pathogenic variants for their impact on the PRRT2 interactions with voltage-gated Na^+ channels. We identified two pathogenic mutants with opposite phenotypes on Nav1.2 channels that further strengthen the key role played by voltage-gated Na^+ channels in the hyperexcitability underlying the paroxysmal manifestations in PRRT2 patients and mechanistically explain the therapeutic efficacy of Na^+ channel blockers in these diseases. The results may help understanding the molecular bases of the inhibitory effects of PRRT2 on neuronal excitability and the pathogenetic mechanisms leading to paroxysmal attacks in PRRT2 patients.

CRediT authorship contribution statement

Bruno Sterlini: Investigation, Methodology, Data curation. **Francesca Franchi:** Investigation, Methodology, Data curation. **Lisastella Morinelli:** Investigation, Methodology, Data curation. **Beatrice Corradi:** Methodology, Data curation. **Chiara Parodi:** Methodology. **Martina Albini:** Methodology. **Alessandra Bianchi:** Methodology. **Antonella Marte:** Methodology, Supervision. **Pietro Baldelli:** Methodology, Data curation. **Giulio Alberini:** Supervision, Data curation. **Luca Maragliano:** Supervision, Data curation, Writing – review & editing. **Pierluigi Valente:** Conceptualization, Supervision, Data curation, Writing – review & editing. **Fabio Benfenati:** Conceptualization, Supervision, Writing – original draft, Funding acquisition. **Anna**

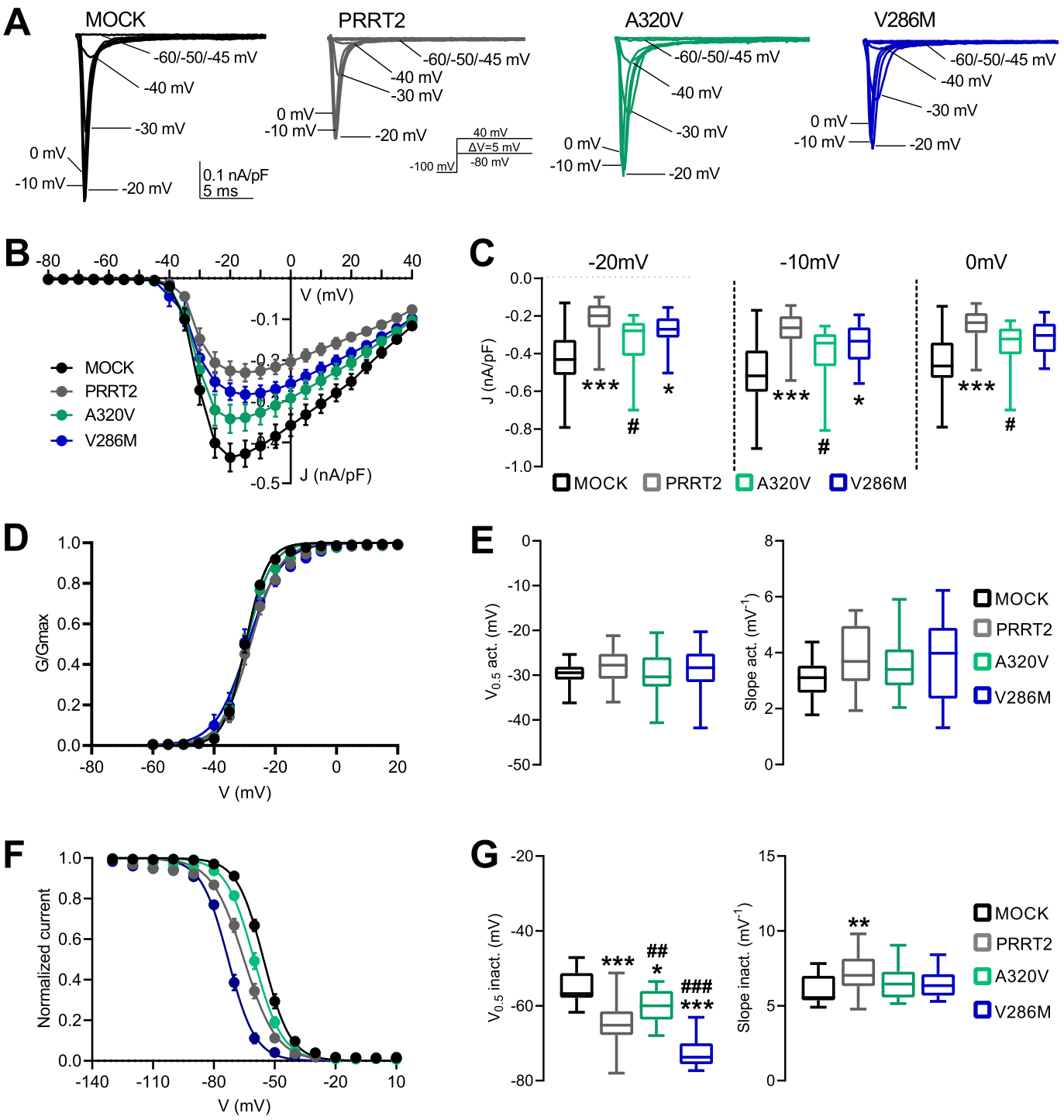

Fig. 6. Effects of the V286M and A320V mutants of PRRT2 on the transient Na^+ current and biophysical properties of Nav1.2 channels.
A-C. Macroscopic Na^+ current. A. Representative whole-cell Na^+ current density (J) traces recorded from Hek293-Nav1.2 transiently transfected with the empty pKH3 control plasmid (black), WT-PRRT2 (grey), A320V PRRT2 (green) or V286M PRRT2 (light blue). Currents were elicited by 5 mV depolarizing step from −80 mV to 40 mV and cells were held at −100 mV (inset). B. Current density to voltage relationship for conditions as in A. C. Box plots of the J values at three representative voltages (−20/−10/0 mV). Data are shown as means ± sem (MOCK, $n = 21$; PRRT2, $n = 20$; A320V $n = 19$; V286M $n = 18$).
D,E. Voltage-dependence of activation. The lines are the best-fitted Boltzmann curves (D). Box plots of the half-maximal voltage of activation ($V_{0.5}$ act) and slope (E). Data are shown as means ± sem (MOCK, n = 21; PRRT2, n = 20; A320V n = 19; V286M n = 18).
F,G. Steady-state inactivation curves. The lines are the best-fitted Boltzmann curves (F). Box plots of the half-maximal voltages for inactivation ($V_{0.5\ inact}$) and slopes (G). (MOCK, n = 21; PRRT2, $n = 27$; A320V n = 18; V286M $n = 14$). *$p < 0.05$, **$p < 0.01$, ***$p < 0.001$ vs MOCK; $^{\#}p < 0.05$, $^{\#\#}p < 0.01$, $^{\#\#\#}p < 0.001$ vs WT-PRRT2; one-way ANOVA/Tukey's tests. (For interpretation of the references to colour in this figure legend, the reader is referred to the web version of this article.)

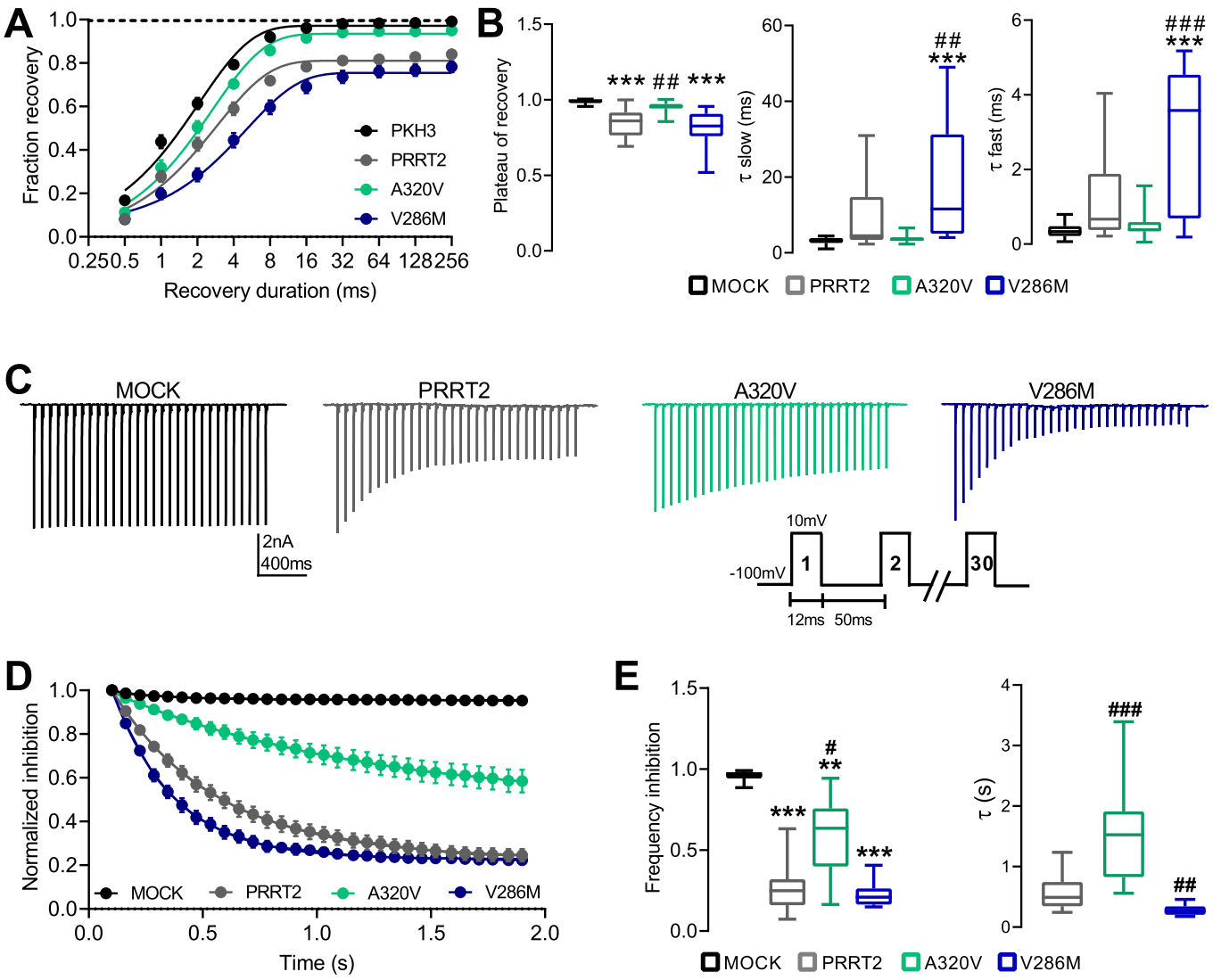

Fig. 7. Effects of the V286M and A320V PRRT2 mutants on the recovery from inactivation of Nav1.2 channels.
A,B. Time-courses of the recovery from inactivation of peak currents at −100 mV recorded in Hek293 cells stably expressing Nav1.2 and transiently transfected with empty vector (MOCK, black), PRRT2 (grey), A320V (green) or V286M (light blue) and plotted on a semi-logarithmic scale (A). Box plots of τ and plateau of recovery estimated from two-phase decay fit to the data (B). (MOCK, $n = 22$; PRRT2, $n = 24$; A320V n = 22; V286M n = 18).
C-E. Frequency-dependent inhibition. C. Representative whole-cell currents recordings in the four experimental conditions shown in A. Frequency-dependent inhibition was determined using a depolarizing pulse to 10 mV from a holding potential of −100 mV for 12 ms at a frequency of 20 Hz. Peak current was normalized to the first pulse in each experiment. D. Time-course of the frequency-dependent inhibition for the genotypes described in A. E. Box plots of the plateau and the τ values estimated from one-phase decay fit to the data. (MOCK, $n = 23$; PRRT2, n = 24; A320V, n = 19; V286M, n = 14). **p < 0.01, ***p < 0.001 vs MOCK; $^{\#}p < 0.05$, $^{\#\#}p < 0.01$, $^{\#\#\#}p < 0.001$ vs WT-PRRT2; one-way ANOVA/Tukey's tests (B) and Kruskal-Wallis/Dunn's tests (E). (For interpretation of the references to colour in this figure legend, the reader is referred to the web version of this article.)

Table 2
Summary of the loss or gain of function of the A320V and V286M mutants with respect to wild-type PRRT2.

PHYSIOLOGICAL EFFECT	EXPERIMENT	MUTANT PHENOTYPE	
		A320V	V286M
Nav1.2 BINDING	Nav1.2 pull-down	LOF	GOF
Nav1.2 MEMBRANE EXPOSURE	Biotinylation	LOF	NS
Na^+ CURRENT	Patch-clamp	LOF	NS
ACTIVATION KINETICS		NS	NS
INACTIVATION KINETICS		LOF	GOF
RECOVERY FROM INACTIVATION		LOF	GOF
PLATEAU INHIBITION	Frequency inhibition	LOF	NS
INHIBITION KINETICS		LOF	GOF

LOF, loss of function; GOF, gain of function; NS, non-significant.

Corradi: Conceptualization, Supervision, Writing – original draft.

Declaration of Competing Interest

The authors declare that they have no conflicts of interest with the contents of this article.

Data availability

The data included in this paper will be made available on request.

Acknowledgements

We are grateful to Dr. Marzia Lecchi (Dept. of Biotechnology and Biosciences, University of Milano-Bicocca) for kindly providing stable

Hek293 clones expressing Nav1.2 channels. We also thank Drs. Riccardo Navone, Arta Mehilli, and Diego Moruzzo (Istituto Italiano di Tecnologia, Genova, Italy) and Silvia Casagrande (University of Genova) for their help in cell cultures and Drs. Ilaria Dallorto, Rossana Ciancio and Annalisa Furlan (Istituto Italiano di Tecnologia and University of Genova) for administrative assistance. The study was supported by Telethon-Italy (Grant GGP19120 to FB). Research grants from IRCCS Ospedale Policlinico San Martino Genova (Ricerca Corrente and "5 × 1000" to AC, PV, PB, and FB), the Compagnia di San Paolo Torino (2015.0546 to FB), the Italian Ministry of University and Research (PRIN2017-A9MK4R to FB and #NEXTGENERATIONEU National Recovery and Resilience Plan (NRRP), project MNESYS PE0000006 – A Multiscale integrated approach to the study of the nervous system in health and disease DN. 1553 11.10.2022 to AC and PB) are also acknowledged. Computing resources were granted by the CINECA supercomputing center under the ISCRA initiative (project HP10CJDOWA). We also gratefully acknowledge the HPC infrastructure and the Support Team at Fondazione Istituto Italiano di Tecnologia.

Appendix A. Supplementary data

Supplementary data to this article can be found online at https://doi.org/10.1016/j.nbd.2023.106177.

References

Andersen, H., 1983. Rattle: a "velocity" version of the shake algorithm for molecular dynamics calculations. J. Comput. Phys. 52, 24–34.
Balagura, G., Riva, A., Marchese, F., Iacomino, M., Madia, F., Giacomini, T., Mancardi, M.M., Amadori, E., Vari, M.S., Salpietro, V., et al., 2020. Clinical spectrum and genotype-phenotype correlations in PRRT2 Italian patients. Eur. J. Pediatr. Neurol. 28, 193–197.
Balusek, C., Hwang, H., Lau, C.H., Lundquist, K., Hazel, A., Pavlova, A., Lynch, D.L., Reggio, P.H., Wang, Y., Gumbart, J.C., 2019. Accelerating membrane simulations with hydrogen mass repartitioning. J. Chem. Theory Comput. 15, 4673–4686.
Binda, F., Valente, P., Marte, A., Baldelli, P., Benfenati, F., 2021. Increased responsiveness at the cerebellar input stage in the PRRT2 knockout model of paroxysmal kinesigenic dyskinesia. Neurobiol. Dis. 152, 105275.
Brooks, B.R., Brooks 3rd, C.L., Mackerell Jr., A.D., Nilsson, L., Petrella, R.J., Roux, B., Won, Y., Archontis, G., Bartels, C., Boresch, S., et al., 2009. CHARMM: the biomolecular simulation program. J. Comput. Chem. 30, 1545–1614.
Calame, D.J., Xiao, J., Khan, M.M., Hollingsworth, T.J., Xue, Y., Person, A.L., LeDoux, M. S., 2020. Presynaptic PRRT2 deficiency causes cerebellar dysfunction and paroxysmal kinesigenic dyskinesia. Neuroscience 448, 272–286.
Catterall, W.A., Lenaeus, M.J., Gamal El-Din, T.M., 2020. Structure and pharmacology of voltage-gated sodium and calcium channels. Annu. Rev. Pharmacol. Toxicol. 60, 133–154.
Chen, W.-J., Lin, Y., Xiong, Z.-Q., Wei, W., Ni, W., Tan, G.-H., Guo, S.-L., He, J., Chen, Y.-F., Zhang, Q.-J., et al., 2011. Exome sequencing identifies truncating mutations in PRRT2 that cause paroxysmal kinesigenic dyskinesia. Nat. Genet. 43, 1252–1255.
Chou, I.C., Lin, S.S., Lin, W.D., Wang, C.H., Chang, Y.T., Tsai, F.J., Tsai, C.H., 2014. Successful control with carbamazepine of family with paroxysmal kinesigenic dyskinesia of PRRT2 mutation. Biomedicine 4, 15.
Coleman, J., Jouannot, O., Ramakrishnan, S.K., Zanetti, M.N., Wang, J., Salpietro, V., Houlden, H., Rothman, J.E., Krishnakumar, S.S., 2018. PRRT2 regulates synaptic fusion by directly modulating SNARE complex assembly. Cell Rep. 22, 820–831.
Dale, R.C., Gardiner, A., Branson, J.A., Houlden, H., 2014. Benefit of carbamazepine in a patient with hemiplegic migraine associated with PRRT2 mutation. Dev. Med. Child Neurol. 56, 910.
Darden, T., York, D., Pedersen, L., 1993. Particle mesh Ewald: a N-log(N) method for Ewald sums in large systems. J. Chem. Phys. 98, 10089–10092.
Delcourt, M., Riant, F., Mancini, J., Milh, M., Navarro, V., Roze, E., Humbertclaude, V., Korff, C., Des Portes, V., Szepetowski, P., et al., 2015. Severe phenotypic spectrum of biallelic mutations in PRRT2 gene. J. Neurol. Neurosurg. Psychiatry 86, 782–785.
Döring, J.H., Saffari, A., Bast, T., Brockmann, K., Ehrhardt, L., Fazeli, W., Janzarik, W.G., Kluger, G., Muhle, H., Møller, R.S., et al., 2020. The phenotypic spectrum of PRRT2-associated paroxysmal neurologic disorders in childhood. Biomedicines 8, 456.
Döring, J.H., Saffari, A., Bast, T., Brockmann, K., Ehrhardt, L., Fazeli, W., Janzarik, W.G., Klabunde-Cherwon, A., Kluger, G., Muhle, H., et al., 2022. Efficacy, tolerability, and retention of antiseizure medications in prrt2-associated infantile epilepsy. Neurol. Genet. 8, e200020.
Ebrahimi-Fakhari, D., Saffari, A., Westenberger, A., Klein, C., 2015. The evolving spectrum of PRRT2-associated paroxysmal diseases. Brain 138, 3476–3495.
Fang, J., Wang, S., Zhao, G., Cao, L., 2020. Novel mutation of the PRRT2 gene in two cases of paroxysmal kinesigenic dyskinesia: two case reports. Biomed. Rep. 12, 309–312.
Feller, S.E., Zhang, Y., Pastor, R.W., Brooks, B.R., 1995. Constant pressure molecular dynamics simulation: the Langevin piston method. J. Chem. Phys. 103, 11.
Ferrante, D., Sterlini, B., Prestigio, C., Marte, A., Corradi, A., Onofri, F., Tortarolo, G., Vicidomini, G., Petretto, A., Muià, J., et al., 2021. PRRT2 modulates presynaptic Ca^{2+} influx by interacting with P/Q-type channels. Cell Rep. 35, 109248.
Forrest, M.P., Dos Santos, M., Piguel, N.H., Wang, Y.-Z., Hawkins, N.A., Bagchi, V.A., Dionisio, L.E., Yoon, S., Simkin, D., Martin-de-Saavedra, M.D., et al., 2023. Rescue of neuropsychiatric phenotypes in a mouse model of 16p11.2 duplication syndrome by genetic correction of an epilepsy network hub. Nat. Commun. 14, 825.
Franchi, F., Marte, A., Corradi, B., Sterlini, B., Alberini, G., Romei, A., De Fusco, A., Vogel, A., Maragliano, L., Baldelli, P., et al., 2023. The intramembrane COOH-terminal domain of PRRT2 regulates voltage-dependent Na^+ channels. J. Biol. Chem. 299, 104632.
Fruscione, F., Valente, P., Sterlini, B., Romei, A., Baldassari, S., Fadda, M., Prestigio, C., Giansante, G., Sartorelli, J., Rossi, P., et al., 2018. PRRT2 controls neuronal excitability by negatively modulating Na^+ channel 1.2/1.6 activity. Brain 141, 1000–1016.
Gardiner, A.R., Jaffer, F., Dale, R.C., Labrum, R., Erro, R., Meyer, E., Xiromerisiou, G., Stamelou, M., Walker, M., Kullmann, D., et al., 2015. The clinical and genetic heterogeneity of paroxysmal dyskinesias. Brain 138, 3567–3580.
Guerrini, R., Conti, V., Mantegazza, M., Balestrini, S., Galanopoulou, A.S., Benfenati, F., 2022. Developmental and epileptic encephalopathies: from genetic heterogeneity to phenotypic continuum. Physiol. Rev. 103, 433–513.
Hopkins, C., Le Grand, S., Walker, R., Roitberg, A., 2015. Long-time-step molecular dynamics through hydrogen mass repartitioning. J. Chem. Theory Comput. 11, 1864–1874.
Huang, X.J., Wang, T., Wang, J.L., Liu, X.L., Che, X.Q., Li, J., Mao, X., Zhang, M., Bi, G. H., Wu, L., et al., 2015. Paroxysmal kinesigenic dyskinesia: clinical and genetic analyses of 110 patients. Neurology 85, 1546–1553.
Huang, J., Rauscher, S., Nawrocki, G., Ran, T., Feig, M., de Groot, B., Grubmüller, H., MacKerell, A., 2017. CHARMM36: an improved force field for folded and intrinsically disordered proteins. Biophys. J. 112, 175a–176a.
Humphrey, W., Dalke, A., Schulten, K., 1996. VMD - Visual Molecular Dynamics. J. Mol. Graph. 14, 33–38.
Jo, S., Kim, T., Lyer, V.G., Im, W., 2008. CHARMM-GUI: a web-based graphical user interface for CHARMM. J. Comput. Chem. 29, 1859–1865.
Jumper, J., Evans, R., Pritzel, A., Green, T., Figurnov, M., Ronneberger, O., Tunyasuvunakool, K., Bates, R., Žídek, A., Potapenko, A., et al., 2021. Highly accurate protein structure prediction with AlphaFold. Nature 596, 583–589.
Labate, A., Tarantino, P., Viri, M., Mumoli, L., Gagliardi, M., Romeo, A., Zara, F., Annesi, G., Gambardella, A., 2012. Homozygous c.649dupC mutation in PRRT2 worsens the BFIS/PKD phenotype with mental retardation, episodic ataxia, and absences. Epilepsia 53, e196–e199.
Lee, H.Y., Huang, Y., Bruneau, N., Roll, P., Roberson, E.D., Hermann, M., Quinn, E., Maas, J., Edwards, R., Ashizawa, T., et al., 2012. Mutations in the gene PRRT2 cause paroxysmal kinesigenic dyskinesia with infantile convulsions. Cell Rep. 1, 2–12.
Lee, J., Cheng, X., Swails, J.M., Yeom, M.S., Eastman, P.K., Lemkul, J.A., Wei, S., Buckner, J., Jeong, J.C., Qi, Y., et al., 2016. CHARMM-GUI input generator for NAMD, GROMACS, AMBER, OpenMM, and CHARMM/OpenMM simulations using the CHARMM36 additive force field. J. Chem. Theory Comput. 12, 405–413.
Lerche, H., 2018. Synaptic or ion channel modifier? PRRT2 is a chameleon-like regulator of neuronal excitability. Brain 141, 938–941.
Li, M., Niu, F., Zhu, X., Wu, X., Shen, N., Peng, X., Liu, Y., 2015. PRRT2 mutant leads to dysfunction of glutamate signaling. Int. J. Mol. Sci. 16, 9134–9151.
Li, H.F., Yang, L., Yin, D., Chen, W.J., Liu, G.L., Ni, W., Wang, N., Yu, W., Wu, Z.Y., Wang, Z., 2019. Associations between neuroanatomical abnormality and motor symptoms in paroxysmal kinesigenic dyskinesia. Parkinsonism Relat. Disord. 62, 134–140.
Liu, Y.T., Nian, F.S., Chou, W.J., Tai, C.Y., Kwan, S.Y., Chen, C., Kuo, P.W., Lin, P.H., Chen, C.Y., Huang, C.W., et al., 2016. PRRT2 mutations lead to neuronal dysfunction and neurodevelopmental defects. Oncotarget 7, 39184–39196.
Lomize, M.A., Pogozheva, I.D., Joo, H., Mosberg, H.I., Lomize, A.L., 2012. OPM database and PPM web server: resources for positioning of proteins in membranes. Nucleic Acids Res. 40, D370–D376.
Lu, J.G., Bishop, J., Cheyette, S., Zhulin, I.B., Guo, S., Sobreira, N., Brenner, S.E., 2018. A novel PRRT2 pathogenic variant in a family with paroxysmal kinesigenic dyskinesia and benign familial infantile seizures. Cold Spring Harb. Mol. Case Stud. 4, a002287.
Lu, B., Lou, S.S., Xu, R.S., Kong, D.L., Wu, R.J., Zhang, J., Zhuang, L., Wu, X.M., He, J.Y., Wu, Z.Y., et al., 2021. Cerebellar spreading depolarization mediates paroxysmal movement disorder. Cell Rep. 36, 109743.
Mantegazza, M., Cestèle, S., Catterall, W.A., 2021. Sodium channelopathies of skeletal muscle and brain. Physiol. Rev. 101, 1633–1689.
Merrick, E.C., Kalmar, C.L., Snyder, S.L., Cusdin, F.S., Yu, E.J., Sando, J.J., Isakson, B.E., Jackson, A.P., Patel, M.K., 2010. The importance of serine 161 in the sodium channel beta3 subunit for modulation of Na(V)1.2 gating. Pflugers Arch. 460, 743–753.
Michetti, C., Castroflorio, E., Marchionni, I., Forte, N., Sterlini, B., Binda, F., Fruscione, F., Baldelli, P., Valtorta, F., Zara, F., et al., 2017a. The PRRT2 knockout mouse recapitulates the neurological diseases associated with PRRT2 mutations. Neurobiol. Dis. 99, 66–83.
Michetti, C., Corradi, A., Benfenati, F., 2017b. PRRT2, a network stability gene. Oncotarget 8, 55770–55771.
Mo, J., Wang, B., Zhu, X., Wu, X., Liu, Y., 2019. PRRT2 deficiency induces paroxysmal kinesigenic dyskinesia by influencing synaptic function in the primary motor cortex of rats. Neurobiol. Dis. 121, 274–285.
Neria, E., Fischer, S., Karplus, M., 1996. Simulation of activation free energies in molecular systems. J. Chem. Phys. 105, 1902–1921.

Pan, Y., Liu, Q., Zhang, J., Yang, Y., Tian, Y., Zeng, J., Yin, P., Mei, L., Xiong, W.C., Li, X. J., et al., 2020. PRRT2 frameshift mutation reduces its mRNA stability resulting loss of function in paroxysmal kinesigenic dyskinesia. Biochem. Biophys. Res. Commun. 522, 553–559.

Phillips, J.C., Hardy, D.J., Maia, J.D., Stone, J., Ribeiro, J.V., Bernardi, R.C., Buch, R., Fiorin, G., Hénin, J., Jian, W., et al., 2020. Scalable molecular dynamics on CPU and GPU architectures with NAMD. J. Chem. Phys. 153, 044130.

Rives, A., Meier, J., Sercu, T., Goyal, S., Lin, Z., Liu, J., Guo, D., Ott, M., Zitnick, C.L., Ma, J., et al., 2021. Biological structure and function emerge from scaling unsupervised learning to 250 million protein sequences. Proc. Natl. Acad. Sci. U. S. A. 118, e2016239118.

Rossi, P., Sterlini, B., Castroflorio, E., Marte, A., Onofri, F., Valtorta, F., Maragliano, L., Corradi, A., Benfenati, F., 2016. A novel topology of proline-rich transmembrane protein 2 (PRRT2): hints for an intracellular function at the synapse. J. Biol. Chem. 291, 6111–6123.

Sterlini, B., Romei, A., Parodi, C., Aprile, D., Oneto, M., Aperia, A., Valente, P., Valtorta, F., Fassio, A., Baldelli, P., et al., 2021. An interaction between PRRT2 and Na^+/K^+ ATPase contributes to the control of neuronal excitability. Cell Death Dis. 12, 292.

Suzuki-Muromoto, S., Kosaki, R., Kosaki, K., Kubota, M., 2020. Familial hemiplegic migraine with a PRRT2 mutation: phenotypic variations and carbamazepine efficacy. Brain Dev. 42, 293–297.

Tan, G.H., Liu, Y.Y., Wang, L., Li, K., Zhang, Z.Q., Li, H.F., Yang, Z.F., Li, Y., Li, D., Wu, M.Y., et al., 2018. PRRT2 deficiency induces paroxysmal kinesigenic dyskinesia by regulating synaptic transmission in cerebellum. Cell Res. 28, 90–110.

Tsai, M.H., Nian, F.S., Hsu, M.H., Liu, W.S., Liu, Y.T., Liu, C., Lin, P.H., Hwang, D.Y., Chuang, Y.C., Tsai, J.W., 2019. PRRT2 missense mutations cluster near C-terminus and frequently lead to protein mislocalization. Epilepsia 60, 807–817.

Valente, P., Castroflorio, E., Rossi, P., Fadda, M., Sterlini, B., Cervigni, R.I., Prestigio, C., Giovedì, S., Onofri, F., Mura, E., et al., 2016. PRRT2 is a key component of the Ca^{2+}-dependent neurotransmitter release machinery. Cell Rep. 15, 117–131.

Valente, P., Romei, A., Fadda, M., Sterlini, B., Lonardoni, D., Forte, N., Fruscione, F., Castroflorio, E., Michetti, C., Giansante, G., et al., 2019. Constitutive inactivation of the PRRT2 gene alters short-term synaptic plasticity and promotes network hyperexcitability in hippocampal neurons. Cereb. Cortex 29, 2010–2033.

Valente, P., Marte, A., Franchi, F., Sterlini, B., Casagrande, S., Corradi, A., Baldelli, P., Benfenati, F., 2022. A push-pull mechanism between PRRT2 and β4-subunit differentially regulates membrane exposure and biophysical properties of NaV1.2 sodium channels. Mol. Neurobiol. 60, 1281–1296.

Valtorta, F., Benfenati, F., Zara, F., Meldolesi, J., 2016. PRRT2: from paroxysmal disorders to regulation of synaptic function. Trends Neurosci. 39, 668–679.

Winters, J.J., Isom, L.L., 2016. Developmental and regulatory functions of Na+ channel non-pore-forming β subunits. Curr. Top. Membr. 78, 315–351.

Wu, L., Tang, H.D., Huang, X.J., Zheng, L., Liu, X.L., Wang, T., Wang, J.Y., Cao, L., Chen, S.D., 2014. PRRT2 truncated mutations lead to nonsense-mediated mRNA decay in paroxysmal Kinesigenic dyskinesia. Parkinsonism Relat. Disord. 20, 1399–1404.

Zhao, S.Y., Li, L.X., Chen, Y.L., Chen, Y.J., Liu, G.L., Dong, H.L., Chen, D.F., Li, H.F., Wu, Z.Y., 2020. Functional study and pathogenicity classification of PRRT2 missense variants in PRRT2-related disorders. CNS Neurosci. Ther. 26, 39–46.

Zhao, Q., Hu, Y., Liu, Z., Fang, S., Zheng, F., Wang, X., Li, F., Li, X., Lin, Z., 2021. PRRT2 variants and effectiveness of various antiepileptic drugs in self-limited familial infantile epilepsy. Seizure 91, 360–368.